

# *In-Vivo* Electrical Impedance Measurement in Mastoid Bone

THOMAS WYSS BALMER <sup>1</sup>, JUAN ANSÓ,<sup>2</sup> ENRIC MUNTANE,<sup>3</sup> KATE GAVAGHAN,<sup>2</sup> STEFAN WEBER,<sup>2</sup>  
ANDREAS STAHEL,<sup>4</sup> and PHILIPPE BÜCHLER<sup>1</sup>

<sup>1</sup>Computational Biomechanics, ISTB, University of Bern, Stauffacherstrasse 78, 3014 Bern, Switzerland; <sup>2</sup>ARTORG Center for Biomedical Engineering, University of Bern, Murtenstrasse 50, 3008 Bern, Switzerland; <sup>3</sup>Control and Sensing Systems Division, CSEM, Rue Jaquet-Droz 1, 2002 Neuchâtel, Switzerland; and <sup>4</sup>Mathematics, Bern University of Applied Sciences, Quellgasse 21, 2501 Biel, Switzerland

(Received 3 June 2016; accepted 3 November 2016; published online 9 November 2016)

Associate Editor Peter E. McHugh oversaw the review of this article.

**Abstract**—Nerve monitoring is a safety mechanism to detect the proximity between surgical instruments and important nerves during surgical bone preparation. In temporal bone, this technique is highly specific and sensitive at distances below 0.1 mm, but remains unreliable for distances above this threshold. A deeper understanding of the patient-specific bone electric properties is required to improve this range of detection. A sheep animal model has been used to characterize bone properties *in vivo*. Impedance measurements have been performed at low frequencies (<1 kHz) between two electrodes placed inside holes drilled into the sheep mastoid bone. An electric circuit composed of a resistor and a Fricke constant phase element was able to accurately describe the experimental measurements. Bone resistivity was shown to be linearly dependent on the inter-electrode distance and the local bone density. Based on this model, the amount of bone material between the electrodes could be predicted with an error of 0.7 mm. Our results indicate that bone could be described as an ideal resistor while the electrochemical processes at the electrode-tissue interface are characterized by a constant phase element. These results should help increasing the safety of surgical drilling procedures by better predicting the distance to critical nerve structures.

**Keywords**—Facial nerve monitoring, Resistivity, Cochlear implant, Nerve preservation.

## INTRODUCTION

Cochlear implantation is a successful treatment for profound to severe hearing loss, especially in children when the operation is conducted early.<sup>12</sup> However, the state of the art surgical procedure required for elec-

trode implantation into the cochlea, includes an invasive mastoidectomy during which the mastoid bone is milled out. The large surgical opening (30–40 mm) enables direct line of sight of vital structures that need to be preserved (e.g. the facial nerve) during surgical access to the cochlea. In the last decade a novel surgical procedure has been proposed to replace mastoidectomy by a minimally invasive access to the cochlea (~1.5 mm). The approach is performed by accurate (<0.3 mm) image-guided drilling systems that rely on preoperative planning and intraoperative navigation.<sup>3,36</sup> The main challenge of this approach is the submillimeter distance range (0.3–1 mm) from the facial nerve to the drilling path. If a drill positioning error occurs (e.g. patient registration error), the facial nerve could be at risk of iatrogenic injury,<sup>21</sup> which must be avoided at any cost. Thereof, a method that can indicate facial nerve proximity independent of navigation could enable robotic cochlear implantation as a clinically safe alternative to mastoidectomy.

Almost four decades ago, Delgado *et al.*<sup>7</sup> proposed nerve monitoring (NM) as a mechanism to protect the facial nerve during cranial base surgery. Since then, this technique has been extensively used and described.<sup>24,25,33,34</sup> Specifically, a pulsed electric current or voltage is imposed between a cathode and a reference anode placed on a location relatively far from the surgical field (typically on the patient's chest). The stimulating electrode is either integrated in a probe or in a cutting tool (e.g. milling bur<sup>5</sup>). When the distance between the instrument and the nerve decreases below a critical level, an action potential will be triggered in the nerve that will result in a measurable contraction of the innervated facial muscles. At electrode to nerve distances from 0 to 2 mm, a current

Address correspondence to Thomas Wyss Balmer, Computational Biomechanics, ISTB, University of Bern, Stauffacherstrasse 78, 3014 Bern, Switzerland. Electronic mail: thomas.wyss@istb.unibe.ch

intensity of 1–2 mA should be sufficient to produce a positive nerve response. The relationship between the electromyogram response measured in the muscle and the distance between the tip of the drill bit and the nerve can be used to estimate nerve proximity. Today nerve monitoring is frequently employed in a number of surgical domains including spine surgery,<sup>35</sup> skull base surgery<sup>8</sup> and thyroid surgery.<sup>9</sup> During the conventional mastoidectomy approach to cochlear implantation, facial nerve monitoring is often used to aid in confirming the location of the nerve during the conventional mastoidectomy approach.<sup>22</sup> Although still controversial, evidence suggests that this approach is cost effective and reduces the risk of iatrogenic nerve injuries.<sup>15</sup>

Nerve monitoring could be an interesting approach to monitor distance between the drilling path and the facial nerve during minimally invasive (robotic) cochlear implantation, ensuring that any unexpected error in drill position is detected before nerve damage occurs. However specificity and sensitivity of commercially available neuro monitoring systems are insufficient for robotic cochlear implantation.<sup>2</sup> Recently, a nerve monitoring approach for robotic cochlear implantation has been proposed<sup>1</sup> enabling sufficient specificity and sensitivity of FN detection at nerve distances below 0.1 mm. However, consistent estimation of facial nerve proximity for distances larger than 0.1 mm remains a challenge due to the differences in the mastoid bone across patients. Patient specific electrical modeling of the patient's mastoid tissue is required to enhance specificity and sensitivity of nerve proximity detection at large distance (0.1–1 mm).

The electric current at the nerve is directly affected by the conductivity of the tissue between the stimulation electrodes and the nerve itself. But currently this information is not taken into account by the existing neuro-monitoring systems. Electric conduction in bone is complex; the mineralized part of this tissue is an electric insulator, while the current propagates through cavities of the trabecular structure filled with conductive tissues such as interstitial fluids or bone marrow. In addition, the bone morphology and trabecular connectivity differ between subjects. As a result, the amount of stimulation current required to detect the facial nerve is different between patients, even for situations where the distance between the stimulating electrodes and the nerve is identical. Including patient-specific information on the bone tissue—for example obtained from clinical CT scans—is expected to provide a more precise estimation of distance between the electrode and the nerve.

Therefore, a deeper knowledge of the propagation of electric currents within the bone is needed to enable

more reliable facial nerve monitoring for minimally invasive cochlear implantation. Early investigations aimed at characterizing bone resistance within the human body, did not consider bone density and structure. For example, Liboff *et al.*<sup>23</sup> measured the resistance of human cortical bone *in vivo* using two platinum needles, and reported resistance divided by the inter-electrode distance, which doesn't directly describe material properties of the measured samples. More recently, other studies have been conducted to evaluate electrical conductivity of bone and correlate it with bone internal characteristics, such as density and architecture.<sup>29–32</sup> Electrical and dielectric bone properties were measured *ex vivo* on cylindrical samples using two stainless steel electrodes covered with a contacting gel. Results showed that relative permittivity and phase angle have a linear correlation with the bone mineral density. However, these studies have been performed *ex vivo* on isolated bone samples, which limits the possible electric flow and disregards the physiological irrigation fluids present in the body.

Herein this work focuses on the electrical characterization of the mastoid bone as an initial step towards the development of patient specific, sub-millimeter accurate nerve monitoring systems. The objective of this study was to characterize the bone electric properties of the deep mastoid bone *in vivo*. Specifically, we aimed at quantifying the relationship between measured bone impedance, bone density and distance between electrodes and to describe how this relationship is affected by the current magnitude and the frequency of the electric signal.

## MATERIALS AND METHODS

### *In-Vivo Impedance Measurements*

With approval from the local ethics board (Bernese cantonal animal commission, approval number 57/12) a sheep animal model was used to measure electrical impedance of the deep mastoid bone tissue. A total of three sheep were used for these experiments and for each sheep three to six impedance measurements were performed.

Each subject was first desensitized with 0.1 mg/kg diazepam and 0.1 mg/kg butorphanol administered intravenously. Then, general anesthesia was induced with an intravenous injection of thiopental 2.5%. Endotracheal intubation was performed, whereby the anesthetic state was maintained by isoflurane in 100% oxygen. Ringers lactate solution was administered at a rate of 10 ml/kg/h. Prior to surgery, four fiducial screws were implanted in the mastoid surface of the surgical site to provide later physical registration of the

patient's anatomy. Thereafter, a computer tomography (CT) scan of the animal's head was acquired with a resolution  $0.2 \times 0.2 \times 0.4 \text{ mm}^3$  (Brilliance CT, Philips AG).

In each sheep, electrical impedance was measured between two custom-made electrode probes (Fig. 1). The probes were inserted manually into the mastoid bone in up to six predefined drilled trajectories. The measurement probes were designed with the same geometry of a drill bit used in robotic cochlear implantation (Fig. 1). Each probe had a ring electrode ( $\text{Ø}1.8 \text{ mm} \times 1 \text{ mm}$ ) axially arranged at a distance of 2 mm from its tip. The ring electrodes were made out of 304 stainless steel. The geometrical design of the probe enabled press-fit insertion into the tunnel to maximize contact between the measurement electrodes and the mastoid tissue.

The position and orientation of drilling trajectories were planned preoperatively using the CT images and an otologic planning software.<sup>13</sup> Up to six pairs of parallel holes were drilled in the mastoid bone of each sheep, in close proximity to the facial nerves. The design of the probes prevented them from being positioned less than 6 mm apart. Several configurations have been used, with varying amount of bone tissue between the measurement electrodes (Fig. 2). An image-guided robotic system developed for minimally invasive cochlear implantation<sup>4</sup> was used to drill each pair of tunnels in the vicinity of the facial nerve of the sheep. The five degrees of freedom serial robot is equipped with a tool holder and a stereo camera system that enables high accuracy navigation with a target accuracy below  $0.2 \text{ mm}^3$ .

A dedicated measurement system (MP150, Biopac, US) was used to generate predefined current signals with varying amplitudes and frequencies. The MP150 was chosen because it comes with an isolated current source (STMISOLA, Biopac, US), enabling galvanic isolation between the power mains and the subject. The voltage drop between the two active electrodes was measured with a differential amplifier (DA100C, Biopac, US). Impedance measurements were performed with input currents of 125, 250 and  $500 \mu\text{A}$  at frequencies of 15, 110 and 1.06 kHz. For each frequency the signal was recorded for 128 sinusoidal periods.

After completion of the measurements, the sheep were euthanized. Finally, the temporal bone was excised and imaged with a resolution of  $18 \mu\text{m}$  using a micro-CT device (Scanco  $\mu\text{CT}$  40, Scanco Medical, Switzerland).

#### Characterization of Measurement Setup

An impedance RCL measurement system (PM6306, Fluke, US) was used to characterize the measurement

probes. The probes were connected to a known resistor of either  $0 \Omega$ ,  $10 \Omega$ ,  $100 \Omega$ ,  $1 \text{ k}\Omega$  or  $10 \text{ k}\Omega$ . The impedance measured by the RCL meter was compared to the known value provided by the manufacturer of the resistor. Impedance measurements were conducted at frequencies ranging from 100 Hz to 100 kHz and for voltage amplitude set to either 50 mV, 100 mV, 200 mV, 400 mV, 1 or 2 V. The chosen resistances, frequencies and voltages corresponded to nominal values expected during the *in vivo* impedance measurements.

The accuracy of the complete measurement setup was tested using the same approach. The same measurement protocol was used as the one planned for the *in vivo* study, including electrode probes and Biopac measurement system (MP150 and STMISOLA). For characterization of the probes, the measurement electrodes were connected to several resistors and the impedance measurement of the experimental setup were compared to the known resistor values.

#### Data Analysis

The measured impedance signals were processed in Matlab (Matlab, Mathworks Inc, US). A high pass filter at 10 Hz and low pass filter at 12 kHz were applied to reduce noise as well as a 50 Hz notch filter to suppress mains power artefacts. The magnitude of the sinusoidal voltage and current were determined by fast Fourier transformation. The complex impedance was calculated as the ratio between the measured voltage and the injected current signal.

In this study, bone impedance was assumed to be a function of the inter-electrode distance and average tissue density. For this reason, the position of the electrodes in the bone was calibrated postoperatively using micro-CT images of the extracted bone samples. Spatial position of the tip of each measurement probe was determined by registering the micro-CT images to the clinical CT datasets using the fiducial screws implanted in the mastoid bone. The centroid of each of the ring electrodes was then calculated by subtracting the known axial distance tip-to-ring (2 mm). The final inter-electrode distance  $L$  was computed as the norm of the line intersecting the two ring centroids minus twice the ring radius ( $0.9 \text{ mm} \times 2$ ).

A homogenization process was performed to reduce the complex flow of current within the bone volume to an idealized resistive model (Fig. 3). The homogenization was enabled by a numerical model describing the flow of current between two electrodes placed in a homogenous media. It was used to calculate the mean tissue density  $D_N$ , as well as the equivalent cross section area of this equivalent resistor.

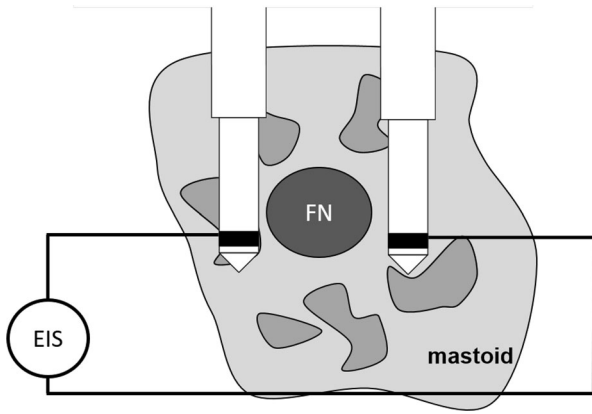


**FIGURE 1.** Schematic description of the impedance measurement concept. Impedance spectroscopy was used to determine the electric properties of the mastoid bone tissue situated between the electrodes.

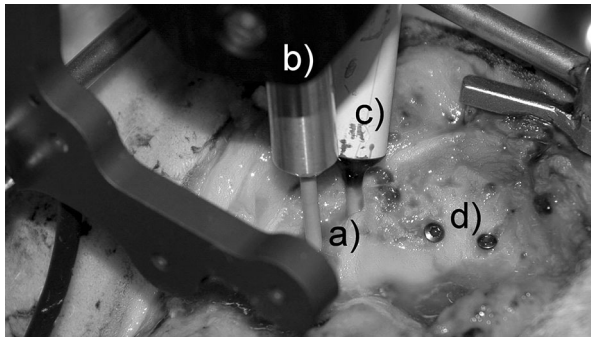


**FIGURE 2.** Two probes used for impedance spectroscopy (a) were inserted into the mastoid bone of the sheep (b). The position of the probes was recorded using an optical tracking system (c) a counter probe was applied to measure impedance (d) four fiducial screws were used to register the physical bone to the optical tracking system and pre-operative images.

The mean tissue density was calculated for each electrode configuration with the hypothesis that the bone resistivity is linearly increasing with its density. Therefore, the mean bone density has been calculated as the weighted average of the local bone density with the electric field generated between the two electrodes (Eqs. 1 and 2). The estimation of the field was based on the assumption that the bone tissue between the electrodes is an isotropic, homogenous material. Solving the equation of electric conduction in the domain surrounding the two electrodes provided the spatial distribution of the electric field:

$$-\sigma \nabla^2 V = 0 \quad (1)$$

$$E = -\nabla V \quad (2)$$

The problem has been solved using the finite element approach to consider a realistic electrode geom-

etry. The commercial finite element package Comsol Multiphysics has been used for the calculations. The ring of the first electrode was set to ground while a voltage of 1 V was applied on the ring of the second electrode. The simulations were performed with a conductivity of 1 S/m, but the results of the homogenization—both for  $D_N$  and  $A$ —are independent from this choice. For each experimental configuration, the numerical model was adapted to reflect the electrode position and the corresponding inter-electrode distance.

For all experimental measurements, the average bone density was estimated as a weighted sum of the local bone Hounsfield value multiplied by the calculated magnitude of the electric field at this location. The weighted average was performed over all voxels around the electrodes. The average bone density was further normalized by the maximal intensity of 1400 Hounsfield units corresponding to dense trabecular bone, which provides a unit-less value between 0 and 1 describing the average bone quality for each electrode configuration;

$$D_N = \frac{1}{1400} \frac{\sum_i \|E_i\| HU_i}{\sum_i \|E_i\|} \quad (3)$$

This finite element model as also be used to estimate an equivalent cross-section area  $A$ . This cross section area corresponds to the area of an idealized resistor producing the same resistance as the material between the two electrodes. For this calculation, we assumed that the ideal resistor has the same resistance as the one calculated with the FE model (i.e. given by the ratio of the calculated current and intensity) and a length identical to the inter-electrode distance;

$$A = \frac{L}{\sigma} \frac{I_{FE}}{V_{FE}} \quad (4)$$

where  $I_{FE}$  and  $V_{FE}$  are respectively the current and voltage between the electrodes obtained with the numerical model and  $L$  is the inter-electrode distance.

### Mathematical Model

An equivalent circuit was used to model the bio-electric properties of the deep mastoid bone tissue. The model was defined as a resistor,  $R$ , in series with a Fricke constant phase element,  $CPE$  (Fig. 4). The complex impedance defined by this circuit is given by:

$$Z = R + \frac{1}{Q_0(j\omega)^n} \quad (5)$$

$$R = \frac{\rho_0 D_N L}{A} \quad (6)$$



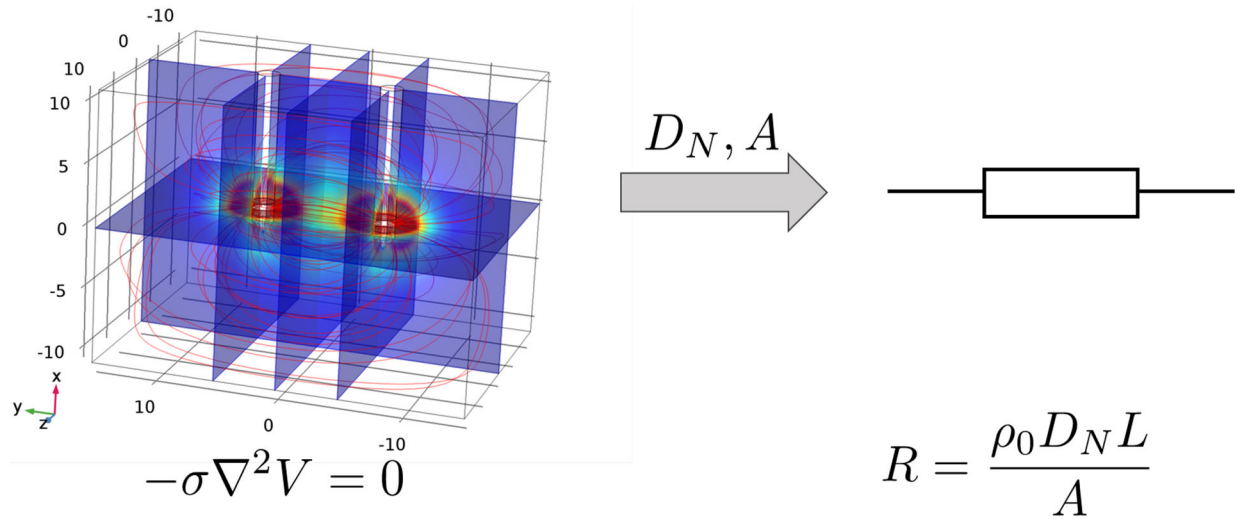


**FIGURE 3.** Finite element simulations were used to determine the parameters of an equivalent model based on an idealized resistor. This homogenization procedure provides the equivalent cross-section area  $A$ , which matches the overall resistance calculated with the finite element model. The numerical simulations were also used to provide an homogenized resistance based on the local bone quality weighted by the electric field at the corresponding spatial location ( $\rho = \rho_0 D_N$ ).

where  $Q_0$  and  $n$  describe the CPE. The parameter  $R$  describes the resistance of the bone tissue, which is assumed to be proportional to the resistivity  $\rho_0$ , the inter-electrode distance  $L$  and the normalized bone quality  $D_N$ . The parameter  $n$  of the CPE directly relate to the phase shift introduced by this component as  $-n \cdot 90^\circ$ . Since  $n$  varies between 0 and 1, the phase lies between 0—pure resistor—and 1 describing a purely capacitive behavior. Similarly, the parameter  $Q_0$  corresponds to a capacitance when  $n$  equals 1 and to the inverse of an idealized resistor when  $n = 0$ . When  $n$  is between 0 and 1, the CPE behaves like a serial circuit of a capacitance and a resistor where the ratio of resistor and capacitive reactance remains constant with changing frequency.

The three model parameters  $\rho_0$ ,  $Q_0$  and  $n$  were determined by fitting the impedance of the circuit to the experimental *in vivo* measurements. In total, the 108 impedance values acquired *in vivo* were used to determine the value of  $\rho_0$ ,  $Q_0$  and  $n$  using a nonlinear least square fitting. For each configuration the inter-electrode distance  $L$ , the averaged bone density  $D_N$  and the cross section area  $A$  were determined based on the planning and imaging (“Data Analysis” section). The cost function was defined as the norm of the difference between the complex experimental impedance and the impedance predicted by the model.

$$\arg \min_{\rho_0, Q_0, n} \|Z_{\text{exp}} - Z(\rho_0, Q_0, n)\| \quad (7)$$

The non-linear least square fitting “Isqnonlin” of Matlab has been used for the calculation. This function relies on the Trust-Region-Reflective Algo-

rithm and was run with the default parameters. The standard error on the estimated model parameters was also provided during the evaluation. To evaluate the goodness of the fitting, the correlation between the magnitudes of the experimental impedance and the corresponding model impedance was evaluated. The coefficient of determination and the  $p$  value were used to quantify the quality of the least square fitting.

To evaluate the ability of the model to predict patient-specific information directly from impedance measurements, the amount of bone material  $P$  between the electrodes was calculated for each of the impedances measured experimentally:

$$P = D_N L \quad (8)$$

This parameter  $P$  was defined as the product of the inter-electrode distance by the normalized density. Using the parameters  $\rho_0$ ,  $Q_0$  and  $n$  previously identified, the patient specific values  $P$  were optimized such as they minimized the norm between the experimental impedance and the impedance predicted by the model (Eq. 9). This minimization approach was required because a direct calculation of the parameter  $P$  using Eqs. (4) and (5), results in a complex value for  $P$ . The reason is that with the model parameter  $\rho_0$ ,  $Q_0$  and  $n$  previously identified, the complex part of the CPE is not exactly the same as the complex part of the experimental measurement. Since  $P$  has to be a real number, it was determined by minimizing the difference between the experimental and model impedance in the complex domain, while ensuring that  $P$  is a real number;

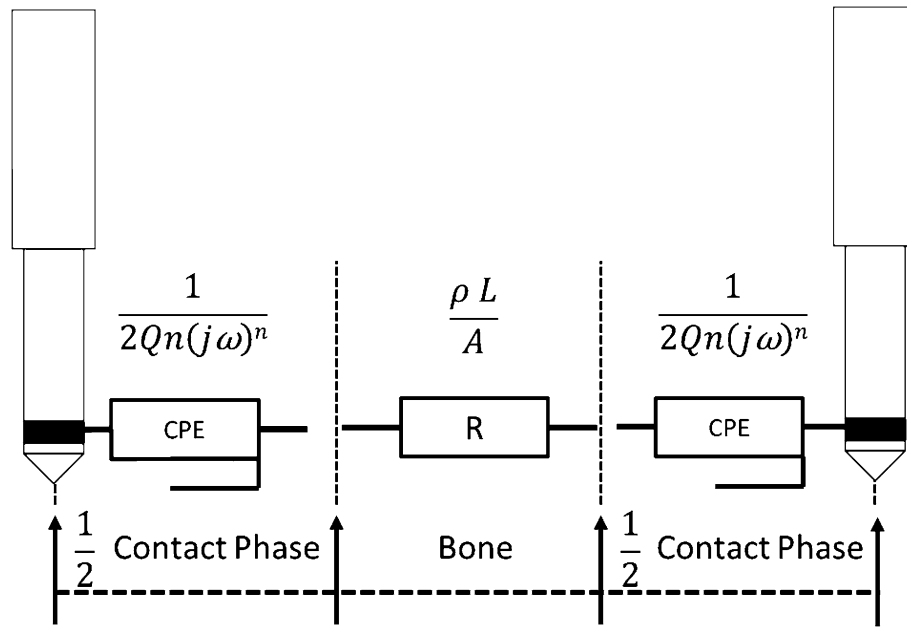


FIGURE 4. Equivalent circuit used to model bone impedance composed of a constant phase element (CPE) in series with resistor  $R$ . The CPE is symmetrically aligned at the contact phase where the steel electrode touches the bone tissue. This model allows to separate the real resistance of the bone from the phase shift introduced by the contact interface.

$$\arg \min_{P \in \mathbb{R}} \|Z_{\text{exp}} - Z(P)\| \quad (9)$$

This minimization has been performed using the “fminsearch” optimization of Matlab, which relies on a Nelder–Mead algorithm. The accuracy of the predictions was analyzed by comparing the patient-specific parameters  $P$  derived from *in vivo* impedance measurements with the corresponding values directly measured on the sheep CT scan (Fig. 7).

## RESULTS

Among the three sheep subjects a total of nine drilled paired tunnels could be used for further analysis, each providing a unique inter-electrode distance as well as one average tissue density. In three cases, the impedance measurement was repeated, which then increased the overall measurement samples to 12. Finally, a total of 108 measurement points (12 measurement configurations  $\times$  3 current amplitudes  $\times$  3 current frequencies) were collected.

### Characterization of the Measurement System

Characterization of the probe indicated that the probe resistance was insignificant compared to the expected bone resistance. The impedance and the phase shift for both probes in series were  $28 \Omega/0.2^\circ$  at 100 Hz and  $28 \Omega/4.0^\circ$  at 1 kHz. The impedance of the

probes was only weakly affected by the measurement frequency with a small increase ( $<4^\circ$ ) of the phase shift from 100 Hz to 1 kHz.

The differential amplifier used by the Biopac system introduced a phase shift caused by the integrated third order Butterworth filter. This low pass filter was not affecting the impedance magnitude, but introduced a significant phase shift in the measured phase for the higher frequencies. The phase shift introduced by the filter could be easily quantified and was found to reach  $0^\circ$  at 15 Hz,  $2.5^\circ$  at 100 Hz and  $22^\circ$  at 1 kHz. Therefore, the combined effect of the phase shift due to the probes and the Biopac system was systematically eliminated from the experimental measurements. Due to its small effect, the impedance of the measurement system was not corrected as it represents approximately only 2% of the actual bone impedance.

### *In Vivo Bone Impedance*

The impedance of the tissue measured *in vivo* covered a large range from 1.0 up to 7.7 k $\Omega$  (Fig. 5). These measurements were also frequency-dependent. As expected, the impedance decreased with the measurement frequency and reached  $1.8 \pm 0.6$  k $\Omega$  at 1 kHz (Fig. 5). The effect of the current magnitude on the measured impedance was smaller than the frequency-dependence. The major effect of the current was observed at 15 Hz ( $\pm 1.27$  k $\Omega$ ), while at higher frequency the impedance measured for high and low current amplitudes differed less than ( $\pm 0.6$  k $\Omega$  at 100 Hz and 1 kHz).

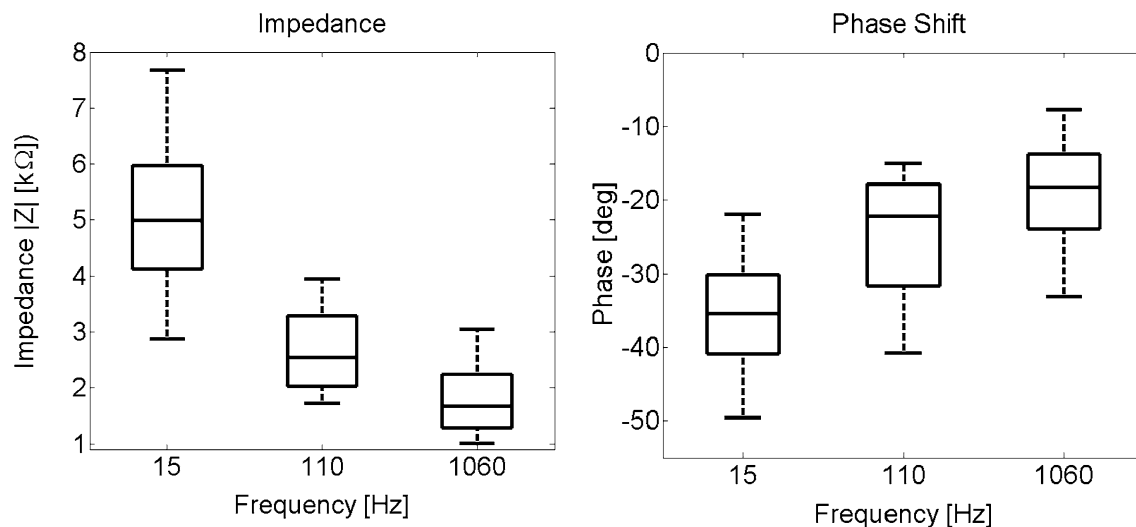


**FIGURE 5.** Magnitude and phase of electrical impedance as a function of the measurement frequency. The bone impedance decreases with the measurement frequency. The variability of the measured impedance was higher at 15 Hz ( $\pm 1.27$  k $\Omega$ ) than at 110 and 1060 Hz ( $\pm 600$   $\Omega$ ). The phase also decreases with the measured frequency from 35° at 15 Hz to 18° at 1060 Hz. The variability is similar for all the three frequencies ( $\pm 7^\circ$ ).

### Model Evaluation

Finite element calculations were used to provide homogenized parameter describing the bone material surrounding the electrode. The bone density corresponding to each electrode positioning was calculated using the weighted average of the Hounsfield unit with the simulated electric field at this position. On the 12 measurement configurations, the average bone density was  $627 \pm 133$  HU, which corresponds to trabecular bone. This homogenization procedure was also used to calculate the equivalent cross section area. The average area for all measured configurations was  $40 \pm 8$  mm<sup>2</sup> (max. area: 53.6 mm<sup>2</sup> and min. area: 33.0 mm<sup>2</sup>), which corresponds to an edge length of about 6.3 mm. The effect of the simulation domain on the resulting homogenized parameters has been evaluated. Results showed that these values become constant for simulation domains larger than 15 mm edge length.

Fitting the impedance measurement in the complex space showed that an electric model was able to describe the experimental measurement with a constant phase element in series with a resistor (Fig. 4). Moreover, results showed that the quality of the model remained good while keeping the parameters of the constant phase element identical for all the measurement configurations (Fig. 6). The least square fitting provides an estimate of the three model parameters as well as the standard error on each of the parameters (Table 1). For all three parameters, the standard error corresponded to about 15% of the value of the parameter (Fig. 5). The quality of the least square fitting was evaluated by comparing the numerical values with the corresponding experimental data points. The

correlation between the numerical and experimental impedance resulted in a coefficient of determination  $R^2 = 0.8$  with  $p$  value  $< 0.001$ , showing that the least square fitting provided reliable representation of the data (Fig. 6).

Finally, the models ability to provide patient-specific information solely based on a single impedance measurement was evaluated. For each of the 108 measurement points, the product of the bone density with the inter-electrode distance  $P$  was calculated using the model and compared with the experimental value (Fig. 7). For this step, the values of  $\rho_0$ ,  $Q_0$  and  $n$  were kept constant and  $P$  was calculated using Eq. 9. The correlation between the model prediction and the experimental values was similar for impedance measured at 100 Hz ( $R^2 = 0.79$ , slope = 1.08,  $p < .001$ ) and 1 kHz ( $R^2 = 0.78$ , slope = 1.03,  $p < .001$ ). However, measurements acquired at 15 Hz showed a lower correlation with the experimental data ( $R^2 = 0.55$ , slope = 1.03,  $p < .001$ ). For the two highest frequencies, the root mean square (RMS) prediction error of  $P$  was about 0.7 mm respectively.

### DISCUSSION

This study reports experimental feasibility, methodology and initial efforts towards a mathematical and bioelectrical model describing *in vivo* electrical resistivity of deep (close to the facial nerve) mastoid bone in the low frequency spectrum ( $< 1$  kHz). The use of a highly accurate surgical robot for cochlear implantation enabled the accurate planning and posi-

tioning of two measuring electrodes at pre-defined locations relative to the facial nerve. The model has shown ability to predict intrinsic mastoid bone tissue properties, as well as inter-electrode distances from measured electrical impedance data.

**TABLE 1. Parameters identified after fitting the model to the experimental measurements.**

$\rho = \rho_0 D_N = 25.4 \pm 3.7 D_N \Omega m$
$Q_0 = 2.2 \cdot 10^{-5} \pm 0.5 \cdot 10^{-5}$
$n = 0.54 \pm 0.05$

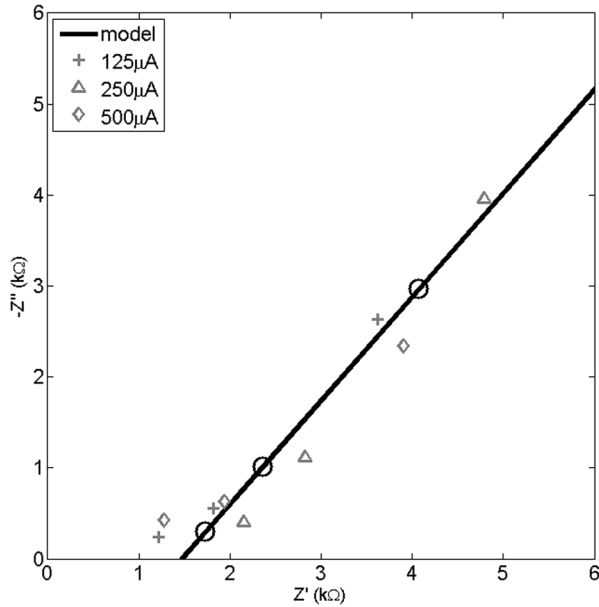


**FIGURE 6. Results of the model fitting plotted for one typical measurement configuration. The Nyquist plot represents the real part of the impedance on the horizontal axis and the complex part on the vertical axis. Therefore, the horizontal intercept represents the resistive element of the model and the slope of the fit corresponds to the phase of the CPE.**

The measured *in vivo* impedance could be described by a simple electrical circuit composed of a resistor in series with a constant phase element. This basic model of the mastoid bone only requires the identification of three parameters. Interestingly, the same set of parameters could be used to describe the behavior of the constant phase element for all of the measured impedance data. The interface between the electrodes and the existing fluids (interstitial, blood, NaCl electrolyte, etc.) may be similar for all the measurement configurations and thus did not depend on the inter-electrode distance nor on the bone density. Therefore, our results support the hypothesis that the constant phase element describes the constant polarization and electrochemical processes occurring at the electrode-tissue interface. On the other hand, the resistor component of the circuit differs for each measurement. This resistance showed a high dependence on average bone quality and inter-electrode distance, which corresponds to the representation of bone tissue as an ideal resistor. Therefore, the model could be used to predict inter-electrode distance based on preoperative CT imaging and intraoperative complex impedance measurements.

The overall relative error of the model impedance was about 20%. Taking into account the manifold uncertainties of the whole *in vivo* measurement procedures, this level of accuracy may be deemed satisfactory as the expected error at nerve distances below 1 mm would be close to 0.2 mm when assuming a linear error function. However, it should be noticed that the accuracy of the measurements also depends on the frequency. Overall, the errors were larger at 15 Hz than at higher frequencies. However, model predictions were similar at 100 Hz and 1 kHz. Therefore, while very low measurements frequencies should be avoided, measurement acquired at a relatively low frequency of 100 Hz would be suitable to achieve

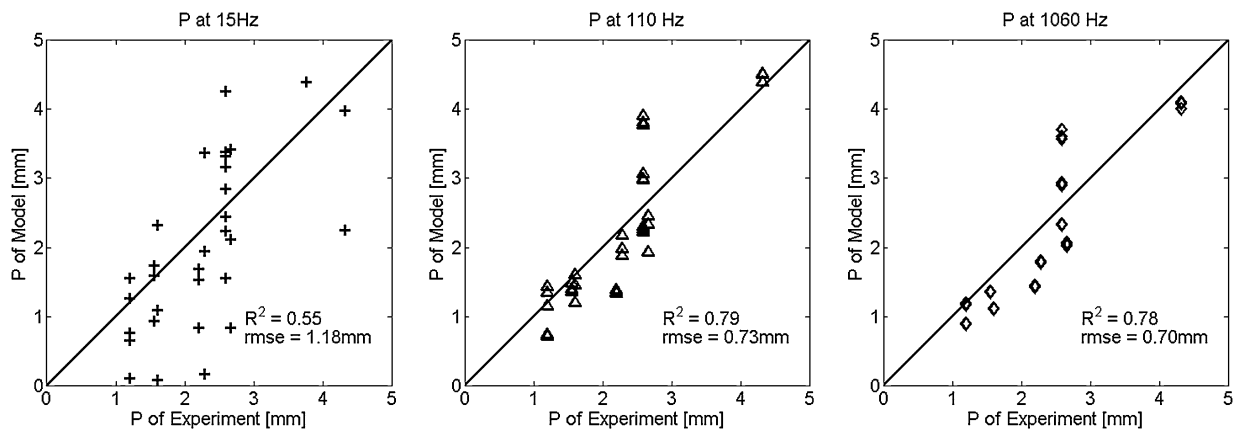


**FIGURE 7. Comparison of the patient-specific parameters ( $D_N L$ ) predicted by the model with the experiment measurements. Each prediction of the model was obtained by a single impedance measurement. The accuracy of the prediction was low at 15 Hz, but a correlation of  $R^2 = 0.79$  and  $R^2 = 0.78$  was obtained at 100 Hz and 1 kHz respectively.**



accurate impedance measurement and eventually for neuro-monitoring applications.

The higher variability of the measurements and predictions observed at 15 Hz than at higher frequencies results from polarization effects. With stainless steel electrodes, it is known that higher electrode–electrolyte polarization occurs at low frequencies.<sup>11,20</sup> This phenomenon has been previously described by several authors such as Schwan *et al.*<sup>26,27</sup> The specific polarization impedance (resistance and capacitance) will depend on the geometry of the electrode, its material as well as the electrolyte composition. In this study, a CPE element has been used to model the electrode–electrolyte polarization interface. However, this simplification is insufficiently to decouple parasitic polarization resistances from the measured data at the lowest measured frequency (15 Hz). A frequency range above 200 kHz has been suggested to be adequate<sup>16–19</sup> to avoid large errors in the estimation of tissue properties using stainless steel needle electrodes, having a similar geometry to the neuro-monitoring electrode probes used in this study. In addition, the electrode–tissue selectivity volume will depend on electrode geometry and surface area. Therefore, the model accuracy should be verified with each specific electrode geometries, and higher frequency bands would likely need to be used for clinical applications.

The resistive part of the model has been described as an idealized resistor proportional to the average bone density and to the inter-electrode distance. While the distance between the electrodes is well defined, the average bone intensity is more difficult to quantify. The bone material around the electrodes is likely to have a stronger contribution to the overall resistance than bone material located away from this line, which is confirmed by the FE simulations. Therefore, local bone density has been weighted according to the local electric field calculated at each spatial position between the two electrodes. This approach enables to account for the relative contribution to the resistivity of each voxel of the bone tissue in the image, but does not require the definition of an arbitrary region of interest around the electrode to average bone intensities. The bone material located far from the electrode will not contribute to the weighted average, since the current density decreases when the distance to the electrode increases. Although this weighted average provides a good estimate of the contribution of each part of the bone to the overall resistance, the current density calculated with the model remains an approximation. Numerical modeling of the current flow accounting for the inhomogeneous bone distribution could be used to improve the model predictions. However, this approach remains challenging since it requires the pre-existing knowledge of bone conductivity which can

only be obtained after fitting the model to the experimental data.

An equivalent cross section has been estimated as part of the homogenization procedure. This parameter depends on the size of the simulation domain, but reached a constant value when the domain edge length is larger than 15 mm. This dimension is sufficiently small for our application, since the region of interest included around the middle and inner ear has a typically size around 15 to 25 mm. This equivalent cross section was necessary to determine the model parameters (i.e. resistivity and constant phase element), but the optimization and the prediction of  $P$  could be performed without determining the cross-section area. However, in this case, it would not be possible to obtain the bone resistivity.

The simplified model used to describe the experimental measurement is composed of a CPE in series with a resistor. This configuration implies that the electrode interface doesn't allow for DC conductance. This is certainly a limitation of this modeling approach. A more realistic model should consider an additional resistor in parallel to the CPE. However, the limited number of frequency time points recorded during the *in vivo* study makes the identification of the value of this additional resistor unreliable, while the simplified model proved to be able to accurately represent the experimental data. To accurately estimate the DC resistance of the tissue, measurement should be performed at lower frequencies, which requires larger integration time and more complex measuring systems. Moreover, in the neuro-monitoring context, DC resistance is of minor interest. For these reasons, this limitation is not critical for this study.

A direct comparison of our results with previous work is difficult. Only few studies have reported *in vivo* bone electric measurements. But although, the bone type and quality could not be directly compared to our sample, our measurements are in range with these previous reports.<sup>10</sup> Sierposwska *et al.*<sup>29–32</sup> performed more detailed analyses of the bone conductivity and its relation to bone density. Although their measurements have been performed *ex vivo* on cylindrical bone samples, the resistivity reported varied between 5  $\Omega\text{m}$  and 14  $\Omega\text{m}$  depending on the density of the trabecular bone. These values are very similar to the resistivity that has been found in this study, which lies between 4 and 13  $\Omega\text{m}$  for  $D_N$  in the range of 0.3 and 0.5.

The bone density has been normalized to the maximal value corresponding to previously reported average CT values of dense bone (~1400 HU). This value of 1400 HU also corresponds to the upper 95% CI limit of dense mastoid bone throughout all subjects of this study. This normalization has only a minor effect on the data analysis of the present study, since normal-

ization was performed only to provide a unit-free measurement of bone quality. However, bone intensity provided by the Hounsfield number is an indirect measure of the bone quality. In addition, it has been shown for biomechanical applications that good predictions of the bone stiffness can only be achieved with a proper calibration of the medical images. This calibration could be simply achieved by including a phantom containing several known concentrations of hydroxyapatite while scanning the patient. Similar limitations apply here. The CT scan data must be calibrated to ensure that the same intensity in the image correspond to the identical bone quality across patients. However, this problem remains limited in our study, because the same scanner with identical scanning parameters has been used for all the sheep.

The measurements have been conducted *in vivo*, which provides a physiological environment. The sheep model has been selected because it has been frequently used in the literature as a suitable animal model for otologic surgical training.<sup>6,14,28</sup> Although the mastoid bone in sheep is not pneumatized, the fallopian canal follows a similar anatomy as in human, with cancellous and cortical bone conforming the majority of tissue around the facial nerve. These *in vivo* measurements also imply technical limitations. For example, use of saline solution to clear the surgical area during drilling and in the drilled holes previous to placement of the measuring probes, could have affected the electric properties of the measured tissue samples. The procedure also limits the range of imaging technique available and prevents use of pre-operative micro-CT scanning with a detailed description of bone volume to total volume ratio as well as bone anisotropic and connectivity information. The acquired postoperative micro-CT images were not suitable for accurate bone characterization, since they already contained all drilled tunnels. Due to the removed bone this imaging modality could only be used to ensure an accurate measurement of the electrode positions.

The model proposed in this study enables the prediction of patient-specific parameters concerning the bone density and electrode distance from a single impedance measurement. This information could be used to increase the safety of a minimally invasive surgical drilling procedure by better understanding the distance to the critical nerve structures. A neuro-monitoring approach based on a bipolar electrode proved to be able to detect nerve proximity within 0.1 mm.<sup>1</sup> However, anatomical variability prevented detection of nerve at larger distances. This study is a first step towards including the local bone density in the quantification of nerve proximity by providing a conductivity model of the mastoid bone surrounding

the facial nerve. Adaptation of the proposed model to a bipolar configuration is expected to improve the accuracy of electrode-to-nerve distance estimation during nerve monitoring using tissue impedance measurements and patient specific computer tomography data.

## FUNDING

This work is part of the HearRestore project, scientifically evaluated by the SNF, financed by the Swiss Confederation, and funded by Nano-Tera.ch.

## REFERENCES

- <sup>1</sup>Ansó, J., C. Dür, K. Gavaghan, H. Rohrbach, N. Gerber, T. Williamson, E. M. Calvo, T. W. Balmer, C. Precht, D. Ferrario, M. S. Dettmer, K. M. Rösler, M. D. Caversaccio, B. Bell, and S. Weber. A neuromonitoring approach to facial nerve preservation during image-guided robotic cochlear implantation. *Otol. Neurotol.* 37:89–98, 2016.
- <sup>2</sup>Ansó, J., C. Stahl, N. Gerber, T. M. Williamson, K. Gavaghan, M. Caversaccio, S. Weber, and B. Bell. Feasibility of using EMG for early detection of the facial nerve during robotic direct cochlear access. *Otol. Neurotol.* 35:545–554, 2014.
- <sup>3</sup>Bell, B., N. Gerber, T. Williamson, K. Gavaghan, W. Wimmer, M. Caversaccio, and S. Weber. *In vitro* accuracy evaluation of image-guided robot system for direct cochlear access. *Otol. Neurotol.* 34:1284–1290, 2013.
- <sup>4</sup>Bell, B., C. Stieger, N. Gerber, A. Arnold, C. Nauer, V. Hamacher, M. Kompis, L. Nolte, M. Caversaccio, and S. Weber. A self-developed and constructed robot for minimally invasive cochlear implantation. *Acta Otolaryngol.* 132:355–360, 2012.
- <sup>5</sup>Bernardeschi, D., N. Meskine, N. AlOtaibi, R. Ablonczy, M. Kalamarides, A. B. Grayeli, and O. Sterkers. Continuous facial nerve stimulating burr for otologic surgeries. *Otol. Neurotol.* 32:1347–1351, 2011.
- <sup>6</sup>Cordero, A., M. del mar Medina, A. Alonso, and T. Labatut. Stapedectomy in sheep: an animal model for surgical training. *Otol. Neurotol.* 32:742–747, 2011.
- <sup>7</sup>Delgado, T. E., W. A. Bucheit, H. R. Rosenholtz, and S. Chrissian. Intraoperative monitoring of facila muscle evoked responses obtained by intracranial stimulation of the facila nerve: a more accurate technique for facila nerve dissection. *Neurosurgery* 4:418–421, 1979.
- <sup>8</sup>Dong, C. C. J., D. B. Macdonald, R. Akagami, B. Westerberg, A. Alkhani, I. Kanaan, and M. Hassounah. Intraoperative facial motor evoked potential monitoring with transcranial electrical stimulation during skull base surgery. *Clin. Neurophysiol.* 116:588–596, 2005.
- <sup>9</sup>Dralle, H., C. Sekulla, K. Lorenz, M. Brauckhoff, and A. Machens. Intraoperative monitoring of the recurrent laryngeal nerve in thyroid surgery. *World J. Surg.* 32:1358–1366, 2008.
- <sup>10</sup>Gabriel, C., S. Gabriel, and E. Corthout. The dielectric properties of biological tissues: I. Literature survey. *Phys. Med. Biol.* 41:2231–2249, 1996.

- <sup>11</sup>Geddes, L. A., C. P. Da Costa, and G. Wise. The impedance of stainless-steel electrodes. *Med. Biol. Eng.* 9:511–521, 1971.
- <sup>12</sup>Geers, A. E., J. G. Nicholas, and A. L. Sedey. Language skills of children with early cochlear implantation. *Ear Hear.* 24:46S–58S, 2003.
- <sup>13</sup>Gerber, N., B. Bell, K. Gavaghan, C. Weisstanner, M. Caversaccio, and S. Weber. Surgical planning tool for robotically assisted hearing aid implantation. *Int. J. Comput. Assist. Radiol. Surg.* 9:11–20, 2014.
- <sup>14</sup>Gurr, A., T. Stark, G. Probst, and S. Dazert. The temporal bone of lamb and pig as an alternative in ENT-education. *Laryngorhinootologie* 89:17–24, 2010.
- <sup>15</sup>Heman-Ackah, S. E., S. Gupta, and A. K. Lalwani. Is facial nerve integrity monitoring of value in chronic ear surgery? *Laryngoscope* 123:2–3, 2013.
- <sup>16</sup>Kalvøy, H. Needle guidance in clinical applications based on electrical impedance. *Ann. Biomed. Eng.* 38:2371–2382, 2010.
- <sup>17</sup>Kalvøy, H., L. Frich, S. Grimnes, O. G. Martinsen, P. K. Hol, and A. Stubhaug. Impedance-based tissue discrimination for needle guidance. *Physiol. Meas.* 30:129–140, 2009.
- <sup>18</sup>Kalvøy, H., P. Høyum, S. Grimnes, and Ø. G. Martinsen. From impedance theory to needle electrode guidance in tissue. *J. Phys. Conf. Ser.* 224:12072, 2010.
- <sup>19</sup>Kalvøy, H., G. K. Johnsen, O. G. Martinsen, and S. Grimnes. New method for separation of electrode polarization impedance from measured tissue impedance. *Open Biomed. Eng. J.* 5:8–13, 2011.
- <sup>20</sup>Kalvøy, H., C. Tronstad, B. Nordbotten, S. Grimnes, and Ø. G. Martinsen. Electrical impedance of stainless steel needle electrodes. *Ann. Biomed. Eng.* 38:2371–2382, 2010.
- <sup>21</sup>Labadie, R. F., R. Balachandran, J. H. Noble, G. S. Blachon, J. E. Mitchell, F. A. Reda, B. M. Dawant, and J. M. Fitzpatrick. Minimally invasive image-guided cochlear implantation surgery: first report of clinical implementation. *Laryngoscope* 124:1915–1922, 2014.
- <sup>22</sup>Leonetti, J. P., G. J. Matz, P. G. Smith, and D. L. Beck. Facial nerve monitoring in otologic surgery: clinical indications and intraoperative technique. *Ann. Otol. Rhinol. Laryngol.* 99:911–918, 1990.
- <sup>23</sup>Liboff, A. R., R. A. Rinaldi, L. S. Lavine, and M. H. Shamos. On electrical conduction in living bone. *Clin. Orthop. Relat. Res.* 106:330–335, 1975.
- <sup>24</sup>Prass, R. Iatrogenic facial nerve injury: the role of facial nerve monitoring. *Otolaryngol. Clin. North Am.* 29:265–275, 1996.
- <sup>25</sup>Prass, R., and H. Lüders. Constant-current versus constant-voltage stimulation. *Neurosurgery* 62:622–623, 1985.
- <sup>26</sup>Schwan, H. Electrode polarization impedance and measurements in biological materials. *Ann. N. Y. Acad. Sci.* 148:191–209, 1968.
- <sup>27</sup>Schwan, H. P. Linear and nonlinear electrode polarization and biological materials. *Ann. Biomed. Eng.* 20:269–288, 1992.
- <sup>28</sup>Seibel, V. A. A., L. Lavinsky, and J. A. P. De Oliveira. Morphometric study of the external and middle ear anatomy in sheep: a possible model for ear experiments. *Clin. Anat.* 19:503–509, 2006.
- <sup>29</sup>Sierpowska, J., M. A. Hakulinen, J. Töyräs, J. S. Day, H. Weinans, I. Kiviranta, J. S. Jurvelin, and R. Lappalainen. Interrelationships between electrical properties and microstructure of human trabecular bone. *Phys. Med. Biol.* 51:5289–5303, 2006.
- <sup>30</sup>Sierpowska, J., M. A. Hakulinen, J. Töyräs, J. S. Day, H. Weinans, J. S. Jurvelin, and R. Lappalainen. Prediction of mechanical properties of human trabecular bone by electrical measurements. *Physiol. Meas.* 26:S119–S131, 2005.
- <sup>31</sup>Sierpowska, J., M. J. Lammi, M. A. Hakulinen, J. S. Jurvelin, R. Lappalainen, and J. Töyräs. Effect of human trabecular bone composition on its electrical properties. *Med. Eng. Phys.* 29:845–852, 2007.
- <sup>32</sup>Sierpowska, J., J. Töyräs, M. A. Hakulinen, S. Saarakkala, J. S. Jurvelin, and R. Lappalainen. Electrical and dielectric properties of bovine trabecular bone—relationships with mechanical properties and mineral density. *Phys. Med. Biol.* 48:775–786, 2003.
- <sup>33</sup>Silverstein, H., and S. Rosenberg. Intraoperative facial nerve monitoring. *Otolaryngol. Clin. North Am.* 24:709–725, 1991.
- <sup>34</sup>Silverstein, H., E. Smouha, and R. Jones. Routine identification of the facial nerve using electrical stimulation during otological and neurotological surgery. *Laryngoscope* 98:726–730, 1988.
- <sup>35</sup>Stecker, M. A review of intraoperative monitoring for spinal surgery. *Surg. Neurol. Int.* 3:174, 2012.
- <sup>36</sup>Wanna, G. B., R. Balachandran, O. Majdani, J. Mitchell, and R. F. Labadie. Percutaneous access to the petrous apex *in vitro* using customized micro-stereotactic frames based on image-guided surgical technology. *Acta Otolaryngol.* 1–6, 2009.